Microgrooves Array on Phase-Change Germanium-Antimony-Tellurium Alloys Nanofilm THz Detector

Qi Song, Wei Chen, Jiachen Yang, Min Zhang, Feilong Gao, Bingyuan Zhang, Bo Dong, *Senior Member, IEEE*, Peiguang Yan, and Yanqing Lu, *Senior Member, IEEE*

***Abstract*—Instead of utilizing commercial detectors and a detection scheme based on 2-D layer semiconductors or surface plasmon enhancement effect, we have developed a novel terahertz (THz) detector consisting of an array of microgrooves. This device combines the exceptional performance of materials with the localized surface plasmon (LSP) effect in a sub-wavelength structure electromagnetic-induced well detector. At room temperature, our device achieves a detectivity (D^*) of 6.3 × 10^8 cm $Hz^{1/2}$ pW^{-1} and a responsivity (Rv) of 3.31 × 10^5 V W^{-1} at 0.1 THz, with a 20 μm line spacing array. Furthermore, the effective detection area of our device is 6.5 × 2 mm, making it much more suitable for practical applications. These high-performance THz wave photodetectors open up possibilities for the effective detection of THz waves, which have wide-ranging applications in areas such as high-capacity communications, THz radar, biological diagnosis, and THz detection.**

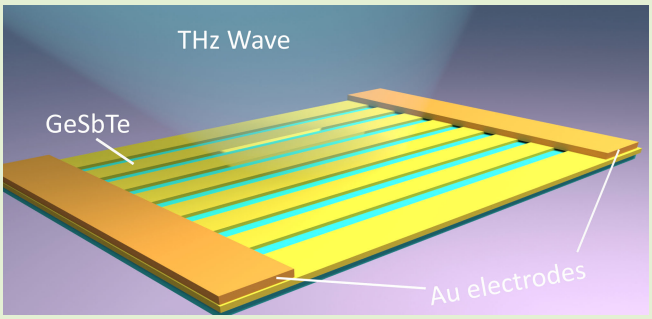

***Index Terms*— Femtosecond laser, optical sensor, terahertz (THz) detector, ultrafast dynamics.**

Manuscript received 16 September 2023; accepted 12 October 2023. Date of publication 23 October 2023; date of current version 30 November 2023. This work was supported in part by NSFC under Grant 12104314 and Grant 62205136; in part by the Key Laboratory of Optoelectronic Devices and Systems of Ministry of Education and Guangdong Province, Research Foundation of Liaocheng University under Grant 318052316; in part by the National Key Research and Development Program of China under Grant 2022YFA1405000; and in part by the Natural Science Foundation of Jiangsu Province, Major Project under Grant BK20212004. The associate editor coordinating the review of this article and approving it for publication was Dr. Amir Ebrahimi. *(Corresponding authors: Wei Chen; Bingyuan Zhang; Min Zhang; Peiguang Yan; Bo Dong.)*

Qi Song, Feilong Gao, and Bingyuan Zhang are with the Shandong Key Laboratory of Optical Communication Science and Technology, School of Physics Science and Information Technology, Liaocheng University, Liaocheng 252059, China (e-mail: zhangbingyuan@lcu.edu.cn).

Wei Chen, Jiachen Yang, and Yanqing Lu are with the National Laboratory of Solid State Microstructures, Key Laboratory of Intelligent Optical Sensing and Manipulation, College of Engineering and Applied Sciences, and the Collaborative Innovation Center of Advanced Microstructures, Nanjing University, Nanjing 210093, China (e-mail: wchen@nju.edu.cn).

Min Zhang and Peiguang Yan are with the Key Laboratory of Optoelectronic Devices and Systems of Ministry of Education and Guangdong Province, College of Physics and Optoelectronic Engineering, Shenzhen University, Shenzhen 518060, China (e-mail: zhangmin@szu.edu.cn; yanpg@szu.edu.cn).

Bo Dong is with the College of Integrated Circuits and Optoelectronic Chips, Shenzhen Technology University, Shenzhen 518118, China (e-mail: dongbo@sztu.edu.cn).

This article has supplementary downloadable material available at https://doi.org/10.1109/JSEN.2023.3324958, provided by the authors.

Digital Object Identifier 10.1109/JSEN.2023.3324958

I. Introduction

HIGH-PERFORMANCE room temperature terahertz (THz) detectors are essential for a wide range of applications. However, current technologies suffer from low sensitivity, narrow spectral bandwidth, complicated structures, and high noise equivalent power (NEP). In the past five years, various room temperature detectors have been reported, categorized into nonlinear hall effect (NHE), thermoelectric effect (TET), field-effect transistor (FET), photogalvanic effects (PCEs), photo-TET (PTE), and surface plasmon polaritons (SPP) enhancement mechanisms [1], [2], [3], [4], [5], [6]. Nevertheless, improving sensitivity and detecting low-energy THz photons at room temperature remains challenging due to the detection mechanisms involved. A novel photoelectric effect-based detector promises high performance and rapid response at room temperature. This detector, with a sub-wavelength size and sandwich structure design, forms an electromagnetically induced well (EIW) in the material when a low-energy THz photon is incident on it [7], [8]. Electrons are injected and captured from the metal layers into the well, altering the material's conductivity and generating a photovoltage signal. The EIW mechanism is particularly suitable for detecting low-energy THz photons at room temperature. To further enhance the performance of the EIW detector, the advantages of bonding materials and surface plasmon enhancement can be combined.

Introducing localized surface plasmon (LSP) through sub-wavelength structures at the metal-medium interface concentrates the energy of the incident electromagnetic field on extremely small scales. This LSP effect, typically achieved through microstructures like wire grids or resonant rings, is crucial for THz detectors. The sensitivity of the device, a crucial aspect for 6G high-speed communication, increases with the longer interaction time or larger active layer that stimulates the photoelectrons with the THz wave. To achieve superior detector performance and boost LSP in the detector, there is an urgent need for thin films that can optimize spectral response. A novel and promising phase-change material (PCM) based on a PCM has emerged as a strategic candidate for the next-generation photoelectric device, surpassing optoelectronically tunable 2-D monolayers [9], [10], [11], [12], [13]. In addition, an important detector of a quartz tuning fork with high performance is reported [39]. Utilizing phase change materials in detector production offers two fundamental benefits. First, these materials exhibit changes in resistivity characteristics during phase transitions, affecting their carrier concentrations and allowing for fine-tuning and optimization of detection sensitivity. Second, during the phase transition, the film examines the structure of various crystalline states, and the introduction of doping enhances the degree of carrier aggregation, resulting in improved detection sensitivity. Among phase change materials, GeSbTe (GST) with a lower crystallization temperature has been widely used in photoelectric device fabrication. GST-based or other Phase change materials-based devices have been reported for integrated plasmonic metamaterials, photo-switching, beam steering, and absorbers [14], [15], [16], [17], [18], [41], [42], [43], [44], [45], [46]. The optical properties of GST films beyond the near-infrared regime, with lossless and high refractive index dielectric properties, make them potential detectors for long wavelengths. Furthermore, GeSbTe exhibits a broad range of resistance variation, excellent oxidation resistance, and favorable scalability. Notably, the resistance of GeSbTe undergoes significant changes between its crystalline and amorphous states. This alteration in resistance can be controlled through the manipulation of the phase change process, rendering GeSbTe highly valuable in memory writing and reading operations. GeSbTe also possesses commendable antioxidant properties, ensuring its stability over prolonged periods of use. The properties of GeSbTe materials can be finely adjusted by modifying their composition and structure to cater to diverse applications. Given these advantages, phase change materials are particularly well-suited for THz detectors that require high stability, superior performance, and multifunctionality.

We have fabricated a new type of GST-based microgrooves array THz device using magnetron sputtering deposition (MSD) combined with the femtosecond laser direct-writing method. This device combines the excellent performance of GST with a larger effective area and the LSP effect in a sub-wavelength structure electromagnetic-induced well detector. In our experiment, the device with a 20 μm line spacing of microgrooves array demonstrates the best performance at room temperature. The detectivity (D^*), NEP, and Rv achieved are 6.3×10^8 cm Hz$^{1/2}$ W^{-1}, 4 pW Hz$^{1/2}$, and 3.31×10^5 V W^{-1} at 0.1 THz, respectively. Furthermore, the effective detection area is 6.5 $\times$ 2 mm, making our device more suitable for practical applications.

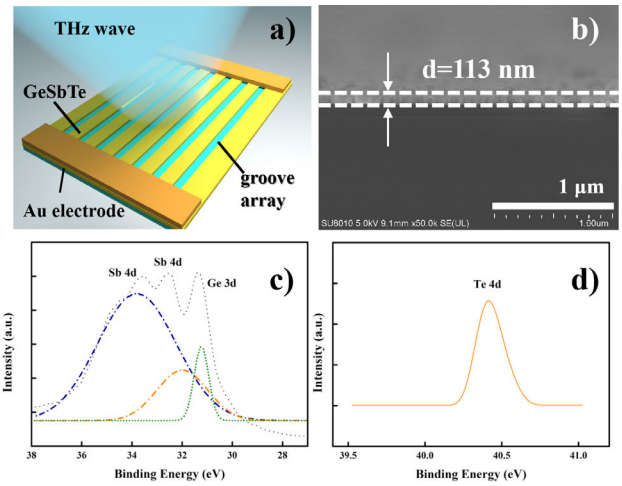

Fig. 1. Device design and characterization. (a) Schematic of the device. (b) Thickness of the GeSbTe film. (c) and (d) XPS results.

II. Characterization, Preparation of Devices, and Experimental Setup

Fig. 1 illustrates the arrangement of ablated grooves made of Germanium-Antimony-Tellurium (GST) on a substrate (silicon covered with a thin 100 nm thickness Au film). The grooves consist of a 113 nm thick GST active layer and a 100 nm thick gold electrode layer, both deposited sequentially on a ~400 μm thick substrate using the MSD technique. The X-ray photoelectron spectroscopy (XPS) analysis of the GeSbTe thin films grown by MSD revealed the binding energies of Ge, Sb, and Te at 31, 32.5, and 40.4 eV, respectively. The fabrication of these devices involved two steps: first, the GST film was prepared using MSD, and second, microgrooves were ablated using a femtosecond laser direct writing system.

The preparation of the GST layer and Au electrode layer involved the following steps: reducing the air pressure to 9×10^{-4} Pa and injecting argon into the cavity, coating the GST target using RF drive mode, and coating the Au target using dc drive mode. For the GST layer, the parameters were set as follows: argon flow rate of 50 state cubic centimeter per minute (SCCM), power of 100 W, and duration time of 150 s. For the Au electrode layer, the parameters were set as follows: argon flow rate of 15 SCCM, current of 0.2 A, and duration time of 90 s. The device design is depicted in Fig. 1(a), while Fig. 1(b) shows photographs of the surface and section of the GeSbTe nanofilm, indicating a thickness of 113 nm. The laser ablation system used a femtosecond laser with a repetition frequency of 50 MHz, pulsewidth of 200 fs, and spot radius of 8 μm. The exposure time was controlled by an electronic shutter, resulting in 25 000 pulses at the minimum on-off time. The sample was placed on a computer-controlled 3-D translation stage, and the scanning speed for the GST film was set at 1 mm/s with a laser power of 120 mW. The SEM pictures revealed a linewidth of 12 μm. The sub-THz emitter employed in these devices was

an impact ionization avalanche transit-time diode (TeraSense impact avalanche and transist time diode (IMPATT) diodes) with a frequency of 0.1 THz. The light and dark currents were recorded using a high-precision picoammeter (Keithley 6485), and a dc power supply (Rigol DP832A) served as the power source. These devices were placed on a tungsten steel probe platform. Experimental details are shown in the Appendix.

III. Results and Discussion

THz waves pose challenges in effectively generating electron-hole pairs in materials due to their low photon energy and the presence of strong background thermal noise. However, in this study, we have successfully addressed this issue by utilizing the electromagnetic induction well effect with a subwavelength structure. This innovative optoelectronic effect is not constrained by the material's bandgap, and its performance is directly influenced by the spacing of the slit [35]. As a result, we have achieved high performance and fast response at room temperature. When THz waves are applied, the photon energy is significantly lower than the bandgap of the semiconductor. As a result, the regular base does not generate electron-hole pairs. However, in structures where the GST layer spacing (channel width) is smaller than the wavelength of the electromagnetic wave, electromagnetic induction wells emerge. These wells allow electrons from the Au layer (also ablated with microgrooves) to be injected into the GST layer and confined in a well state [36].

The exact process can be explained as follows: when a beam of photon-density ϕ_s of THz radiation light is received by the structure, the electric field strength amplitude can be expressed as $E_0 = \phi_s hc_0/(q\lambda^2)$, where h is Planck's constant, c_0 is the speed of light in vacuum, and λ is the wavelength of that THz light wave. This results in an enhanced electric field E_1 within the structure, i.e., $E_1 = \eta E_0$, where $\eta = |(\varepsilon(\omega)(\varepsilon_0\mu_0 k_0^2 - (\pi/a)^2)^{1/2})/((\varepsilon_0\mu_0 k_0^2 - (\pi/a)^2)^{1/2})|$ is the electric field enhancement factor for the active layer spacing, depending on the boundary conditions [37]; ($\varepsilon(\omega)$ is the relative permittivity of the material ε_0 and μ_0 are the permittivity and permeability in vacuum, respectively, and k_0 is the wave vector of the electromagnetic wave in free space, and a is the active layer spacing). Notably, the electric field that causes the electromagnetic induction well effect is not yet E_1 but its antisymmetric electric field E_x (where the active layer spacing is assumed to be in the x-direction), and this antisymmetric electric field is parallel to the surface of the structure. E_x can be written as [35], [37]

$$E_x = E_1 \sin\left(\frac{\pi x}{a}\right) \exp\left(-z\sqrt{\varepsilon_r}\sqrt{\left(\frac{\pi}{a}\right)^2 - k_0^2 - i\omega t}\right). \quad (1)$$

Here, ε_r is the relative permittivity of the semiconductor material, and ω is the angular frequency of the electromagnetic wave. It can be seen from (1), where Ex is a factor that varies with $\exp(i\omega t)$ factor changes. The concentration of electrons in the active layer material is significantly higher than that in the semiconductor. As a result, during the first half of the cycle, the active layer (Au layer) injects electrons into the semiconductor layer, while the electrons are in accelerated motion. In the second half of the cycle, the electrons are decelerated along the track forward due to the opposite direction of the electric field. Consequently, the nonequilibrium electrons do not return to the active layer but instead accumulate in the center of the semiconductor. This phenomenon can be explained by the electromagnetic induction well effect, which provides insights into the characteristics of electron movement and the reason for their confinement in the semiconductor.

Indeed, the explanation of the electromagnetic induction well effect could be further elucidated for better understanding. If the potential angle to analyze can be a more graphic explanation of the electromagnetic induction well, according to the formula $Ex = -\nabla_x \varphi$, can be obtained [37]

$$\varphi = \varphi_1 \cos\left(\frac{\pi x}{a}\right) \exp\left(-z\sqrt{\varepsilon_r}\sqrt{\left(\frac{\pi}{a}\right)^2 - k_0^2 - i\omega t}\right) + c. \quad (2)$$

Here, ϕ_1 is the magnitude of the potential, which also varies with the $\exp(i\omega t)$ factor changes. During the first half cycle, the incident light's antisymmetric electric field creates a potential well, injecting electrons into the semiconductor. These electrons are accelerated from the active layer electrodes at both ends. In the second half cycle, the antisymmetric electric field of the incident light forms a potential barrier. This barrier causes the electrons to decelerate along their original paths, preventing them from returning from one end of the active layer electrodes to another. As a result, the electrons are confined in the EIWs. It is important to note that if the potential barrier is formed in the last half cycle, the electrons will not reverse back to the active layer electrode, so this scenario is not considered [38]. Furthermore, (1) and (2) show that as the z-axis increases, the electric field strength decreases, and the depth of the electromagnetic induction well drops as well.

Due to the different free electron densities of the two materials, the electron injection process mentioned earlier may reach a state of equilibrium after a few cycles of the incident electromagnetic wave [37]. As the injected electrons in the active layer accumulate in the semiconductor, the Fermi energy level is shifted downward. When the device is biased by voltage, the induced electrons will flow along the energy band, allowing for the detection of THz radiation by collecting the photocurrent between the active layer electrodes. Based on the above analysis, it is evident that the spacing of the subwavelength microstructure is a crucial aspect to study. Therefore, our initial focus was on investigating the etching spacing.

Fig. 2 illustrates the performance of devices with varying groove spacing under the same applied voltage. It is observed that for both light current and dark current data, a larger line spacing results in a lower current. This can be attributed to the increased freedom of movement for carriers due to the wider line spacing. Consequently, the number of carriers moving in a specific direction decreases, leading to a reduction in both light and dark currents. As a result, the sensitivity of the corresponding device decreases, and the equivalent noise power of the device improves as the carrier's freedom of movement increases. The performance of the detector also

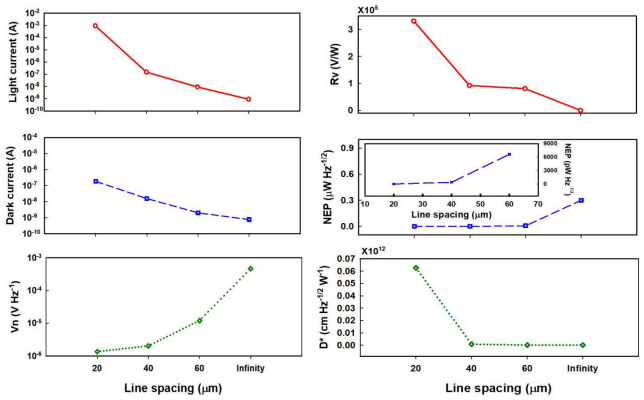

Fig. 2. Performance of devices line spacing versus light current, dark current, *Vn*, *Rv*, NEP, and D^* of the devices at voltage bias of 10 V. Infinity means the GST film without lines.

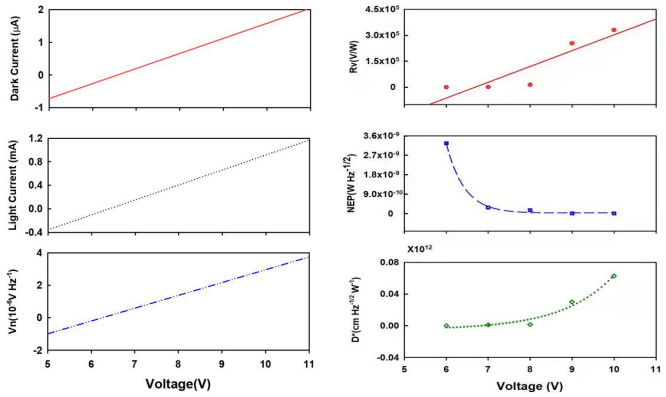

Fig. 3. Light current, dark current, and noise characterization, R_V, NEP, and D^*. Typical calculated (lines) and measured (dots and circles) for 0.1 THz emitter of the 20 μm line spacing device.

diminishes with an increase in line spacing. Based on the findings in Fig. 2, it is determined that the detector with a line spacing of 20 μm exhibits the best performance. Therefore, further research will be conducted using the device with a line spacing of 20 μm. Fig. 3 shows light current, dark current, and noise characterization, R, NEP, and D^* of the 20 μm line spacing device at room temperature. From the dark Ampere-Volt line, a good ohmic character could be observed. The total noise (V_n) of the groove device could be divided into the thermal Johnson–Nyquist noise (V_t) and dark current shot noise (V_b), which can be expressed as [20], [21]

$$v_n = \sqrt{v_t^2 + v_b^2} = \sqrt{4k_B T r + 2q I_d r^2} \tag{3}$$

where k_B is Boltzmann's constant, T is the detector's absolute temperature, r is the resistance value of the device, q is the elementary charge, and I_d is the device's dark current. In addition, the calculated data agrees with the experimental noise level. For 10 V voltage bias, the noise level is $\sim$3 μV Hz$^{-1/2}$. The increasing V_n with increment bias is caused by the dark current shot noise. In addition, the photoresponsivity (R), NEP, and detectivity (D^*) were also used to evaluate the photoelectrical conversion capability of a detector. These figures of merits of R, NEP, and D^* are all calculated by [20] and [22]: $R_V = V/P$, NEP $= v_n/R_V$, and $D^* = \sqrt{S}/\text{NEP}$. Here, I is

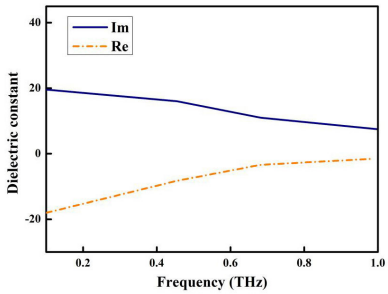

Fig. 4. Real and imaginary parts of the complex dielectric constant dispersion for GST nanofilm.

the photograph current of the device. P is the incident THz power, S is the effective detection area of the detector, and V_n is the noise voltage as shown in (1). Fig. 3 also shows R, NEP, and D^* of the 20 μm line spacing device with different voltages at room temperature for the incident THz frequency of 0.1 THz. Due to the nonequilibrium electrons proportional to the drift velocity, R linearly increases with voltage. With the voltage of 10 V, R of this device is 3.31 $\times$ 10^5 V W^{-1}, which is higher than that of a Golay cell (1 $\times$ 10^5 V W^{-1}). Also, combined with the EIW and LSP effect, our R is also 1.3$\times$ more than the best results of nanostructure devices [21]. The EIW effect makes our device an excellent room temperature detector. In addition, due to increasing noise levels, NEP and D^* show enhancement with the increasing voltage and tend to saturate with the voltage close to 10 V. With the voltage of 10 V, NEP is 4 pW Hz$^{-1/2}$ and just 1/50 more than a commercial Golay cell (140 pW Hz$^{-1/2}$) [20] and 1/3 more than a commercial Schottky diode (15.2 pW Hz$^{-1/2}$) [20].

In order to further explain the working mechanism of our detector, the surface electric field and surface carrier motion are simulated. Fig. 4 shows the complex dielectric constant dispersion for GST devices in the THz spectrum. The real and imaginary parts of the complex dielectric constant dispersion for GST nanofilm are measured by a transmitted THz-TDS. The parameters of femtosecond lasers in THz-TDS are a central wavelength of 780 nm, repetition frequency of 80 MHz, and pulsewidth of 90 fs. Based on the results of the experiment, it is evident that an increase in frequency corresponds to an increase in the real components of the complex dielectric constant, while the imaginary components exhibit a decrease. We used (4) to demonstrate the electronic structure of the ultrathin film devices [23]

$$\varepsilon(\omega) = \frac{i(n+1)c}{\omega d}\frac{1 - T/T_0}{T/T_0} \tag{4}$$

where n is the refractive index, d is the film thickness, c is the speed of light in vacuum, and T/T_0 is the complex transmittance. In addition, we used the Drude model to fit the complex dielectric constant [23]

$$\varepsilon(\omega) = \varepsilon_\infty - \frac{\omega_p^2}{\omega(\omega + i\gamma)} \tag{5}$$

where ε_∞, ω_p, and γ are the dielectric constant for high frequency, plasma frequency, and damping constant, respectively.

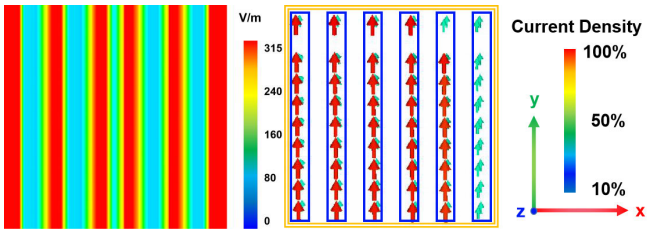

Fig. 5. Surface electric field distribution of the devices of 20 μm line spacing at 0.1 THz (left) and current density distribution and direction on the device surface (right).

The permittivity of the GST films in the THz range is negative according to the Drude model with a temperature of 298 K. Thus, the THz surface plasmons could be excited in GST, which generated the nonequilibrium electrons concomitantly [24], [25]. The simulation results are shown in Fig. 5. The detector combined the surface plasma and THz quantum well. With the THz photon incident, according to the surface plasmon theory, surface plasmons can be generated in the air-GST quantum well structure. After that, these surface plasmons will transfer energies to electrons in GST, resulting in the absorption of incident THz wave by the groove array. The direction perpendicular to the grating plane is defined as z, and E_z is an evanescent wave in the z-direction. The surface plasmon caused by grating coupling forms a standing wave between each groove. There is a large E_z field intensity distribution in the multiquantum well structure area of the detector, and there is a certain non-uniformity in the z-direction. As shown, grooves devices demonstrate a larger intensity of LSPs than the film without grooves. As a consequence, the groove device would absorb more incident photons. The sub-band of the quantum well is slightly lower than the barrier. Therefore, there is a large sub-band transition dipole moment between the first and second sub-bands. With appropriate bias, the excited carriers on the second sub-band are quickly transferred to the continuous state through tunneling and scattering to form the photograph current. Due to the thickness of the whole device in the sub-wavelength scale, the evanescent wave corresponding to the surface plasmon can improve the sub-band absorption efficiency of the device. Employing field enhancement within the groove array could improve the detection efficacy, attributable to the simultaneous induction of more nonequilibrium electrons and augmented absorption of THz waves. Consequently, it improves the response rate and working temperature of the device.

The devices with ablated grooves displayed significantly different dynamics than those without. The responsivity of the devices, with line spacings of 20, 40, and 60 μm, were measured to be 0.331×10^5, 0.90×10^5, and 0.8×10^5 V/W, respectively. The NEP values were found to be 4, 300, and 6000 pW $Hz^{1/2}$, as shown in Fig. 2. These comparative experiments demonstrated that the devices with grooves exhibited a notably high responsivity, which can be attributed to the ablated structure of the devices.

It is well-known that the transient photo-conductivity of semiconductor materials can be influenced by various factors such as morphoses, additional ablated microgrooves, assembled structure, and molecular structure. These factors can trap photo-excited carriers and reduce their recombination velocity. In the case of the groove devices, the ablated lines disrupt the isotopic property, leading to anisotropy in the diffusion range. This, in turn, greatly affects the average mobility of the carriers due to their strong localization on the surface boundaries caused by the surface depletion layer around the lines. The carriers move in the direction of the groove, and therefore,

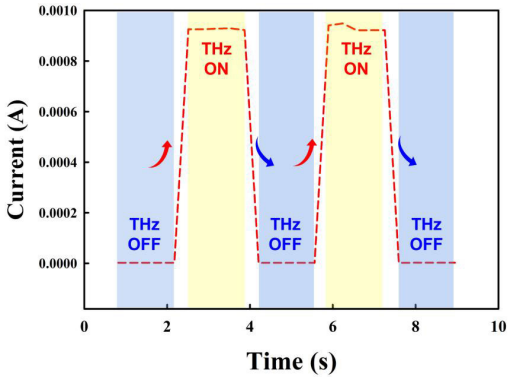

Fig. 6. Switching time of the 20 μm line spacing detector.

TABLE I
THz DETECTORS BASED ON DIFFERENT MATERIALS AND MECHANISMS AT ROOM TEMPERATURE

Materials	Frequency THz	Photoresponsivity V/W	NEP (pW/Hz$^{1/2}$)	Area	Ref
Graphene	0.45	764	34	Nano	1
Graphene transistor	0.12	280	100	Nano	2
Bi_2Se_3	0.3	0.29×10^{-2}	0.36	Nano	7
AlGaN/GaN	0.504	10	25	Nano	4
Selenium doped BP	3.4	3	70000	Nano	30
Self-assembled Sn-nanothreads	0.14	1379	6.5	Nano	31
Bi_2Te_3	0.332	0.74×10^5	1.75	Nano	8
$PtTe_2$	0.12	1400	10	Nano	32
$PdTe_2$	0.3	1.3×10^{-8}	57	Nano	5
Black phosphors(BP)	0.29	297	138	Nano	6
InSb	0.03	2.6×10^5	0.02	Micron	21
Golay cell (Commercial)	0.03-20	1×10^5	140	Millimetre	33
Bolometer (Commercial)	0.15-20	2.4×10^5 (4.2K)	0.25	Millimetre	34
GeSbTe	***0.1***	***3.31×10^5***	***4***	***Millimetre***	***This work***

increasing the line spacing results in an increase in surface defect states, which reduces the recombination velocity of the photo-excited carriers. Consequently, devices with smaller line spacing exhibit higher carrier recombination rates and sensitivity.

Additionally, the response time of the device with a 20 μm line spacing, as shown in Fig. 6, was measured to be 88 ms. Table I lists a comparison of THz detectors based on different materials and mechanisms. It is evident that most detectors are in the form of nanosheets, chemical vapor deposition (CVD) films, or thin crystals in nano or micro dimensions. Detectors with a relatively large effective area are of utmost importance in the fields of THz communication and imaging. Compared to existing detectors, the GST-based microgroove array detector, which demonstrates certain advantages regarding NEP and detection sensitivity, holds significant practical value.

IV. Conclusion

In conclusion, we have conducted an investigation on a high-performance THz wave detector with a large effective area. This detector is based on a microgroove array deposited with GST at room temperature. The combination of GST and the microgroove array results in strong THz wave LSPs, which significantly enhances the detection performance. It is worth noting that the detector performance decreases as the line spacing increases, due to the increased freedom of carrier movement. In our experiment, the best-case scenario with a line spacing of 20 μm achieved a detectivity (D^*) of 6.27×10^8 cm $Hz^{1/2}$ W^{-1} at 0.1 THz, at room temperature. Additionally, we obtained a NEP of 4 pW $Hz^{1/2}$ and a responsivity (Rv) of 3.31×10^5 V W^{-1}. The response time of the device with a 20 μm line spacing was measured to be 88 ms. Remarkably, the effective detection area of our device measures 6.5 $\times$ 2 mm, making it suitable for practical applications. With the enhanced LSP effect and lower crystallization temperature, GST offers significant advantages in fabricating high-performance detectors with large effective areas. Our results demonstrate that large-area THz detectors based on GST can be efficiently fabricated through microstructural design combined with microstructural design, and have the potential to be extended to other novel THz devices.

References

[1] G. Auton et al., "Terahertz detection and imaging using graphene ballistic rectifiers," *Nano Lett.*, vol. 17, no. 11, pp. 7015–7020, Nov. 2017, doi: 10.1021/acs.nanolett.7b03625.

[2] C. Liu et al., "Towards sensitive terahertz detection via thermoelectric manipulation using graphene transistors," *NPG Asia Mater.*, vol. 10, no. 4, pp. 318–327, Apr. 2018, doi: 10.1038/s41427-018-0032-7.

[3] S. Castilla et al., "Fast and sensitive terahertz detection using an antenna-integrated graphene pn junction," *Nano Lett.*, vol. 19, no. 5, pp. 2765–2773, May 2019, doi: 10.1021/acs.nanolett.8b04171.

[4] M. Bauer et al., "A high-sensitivity AlGaN/GaN HEMT terahertz detector with integrated broadband bow-tie antenna," *IEEE Trans. THz Sci. Technol.*, vol. 9, no. 4, pp. 430–444, Jul. 2019, doi: 10.1109/TTHZ.2019.2917782.

[5] C. Guo et al., "Anisotropic ultrasensitive $PdTe_2$-based phototransistor for room-temperature long-wavelength detection," *Sci. Adv.*, vol. 6, no. 36, Sep. 2020, Art. no. eabb6500, doi: 10.1126/sciadv.abb6500.

[6] W. Guo et al., "Sensitive terahertz detection and imaging driven by the photothermoelectric effect in ultrashort-channel black phosphorus devices," *Adv. Sci.*, vol. 7, no. 5, Mar. 2020, Art. no. 1902699, doi: 10.1002/advs.201902699.

[7] Y. Jeong, Y. Bahk, and D. Kim, "Dynamic terahertz plasmonics enabled by phase-change materials," *Adv. Opt. Mater.*, vol. 8, no. 3, Feb. 2020, Art. no. 1900548, doi: 10.1002/adom.201900548.

[8] X. Y. Xu et al., "High responsivity Bi_2Te_3-based room temperature terahertz detector based on metal-semiconductor-metal structure," *J. Infr. Millim. Waves*, vol. 38, no. 4, p. 4459, 2019.

[9] A. Ahmadivand, B. Gerislioglu, and Z. Ramezani, "Generation of magnetoelectric photocurrents using toroidal resonances: A new class of infrared plasmonic photodetectors," *Nanoscale*, vol. 11, no. 27, pp. 13108–13116, Jul. 2019, doi: 10.1039/C9NR04312H.

[10] X. Y. Chen et al., "Reconfigurable and nonvolatile terahertz lithography-free photonic devices based on phase change films," *Photon. Res.*, vol. 11, no. 4, pp. 669–681, 2023, doi: 10.1364/PRJ.478103.

[11] Z. Zheng et al., "Active thermally tunable and highly sensitive terahertz smart windows based on the combination of a metamaterial and phase change material," *Dalton Trans.*, vol. 52, no. 24, pp. 8294–8301, 2023, doi: 10.1039/D3DT00531C.

[12] J. Liu and J. Wei, "Optical nonlinear absorption characteristics of AgInSbTe phase change thin films," *J. Appl. Phys.*, vol. 106, no. 8, Oct. 2009, Art. no. 083112, doi: 10.1063/1.3247194.

[13] Z. Sun, J. Zhou, A. Blomqvist, B. Johansson, and R. Ahuja, "Formation of large voids in the amorphous phase-change memory $Ge_2Sb_2Te_5$ alloy," *Phys. Rev. Lett.*, vol. 102, no. 7, Feb. 2009, Art. no. 075504, doi: 10.1103/PhysRevLett.102.075504.

[14] B. Gerislioglu, G. Bakan, R. Ahuja, J. Adam, Y. K. Mishra, and A. Ahmadivand, "The role of $Ge_2Sb_2Te_5$ in enhancing the performance of functional plasmonic devices," *Mater. Today Phys.*, vol. 12, Mar. 2020, Art. no. 100178, doi: 10.1016/j.mtphys.2020.100178.

[15] W. Dong et al., "Tunable mid-infrared phase-change metasurface," *Adv. Opt. Mater.*, vol. 6, no. 14, Jul. 2018, Art. no. 1701346, doi: 10.1002/adom.201701346.

[16] P. Xu, J. Zheng, J. K. Doylend, and A. Majumdar, "Low-loss and broadband nonvolatile phase-change directional coupler switches," *ACS Photon.*, vol. 6, no. 2, pp. 553–557, Feb. 2019, doi: 10.1021/acsphotonics.8b01628.

[17] C. R. de Galarreta et al., "Nonvolatile reconfigurable phase-change metadevices for beam steering in the near infrared," *Adv. Funct. Mater.*, vol. 28, Mar. 2018, Art. no. 1704993, doi: 10.1002/adfm.201704993.

[18] M. Wuttig, H. Bhaskaran, and T. Taubner, "Phase-change materials for non-volatile photonic applications," *Nature Photon.*, vol. 11, no. 8, pp. 465–476, Aug. 2017, doi: 10.1038/nphoton.2017.126.

[19] R. Kim, H. Kim, K. Park, J. Ahn, and S. Yoon, "Layer-by-layer growth of GeSbTe thin films by metal-organic CVD for phase change memory applications," *Chem. Vapor Deposition*, vol. 15, nos. 10–12, pp. 296–299, Dec. 2009, doi: 10.1002/cvde.200906791.

[20] Q. Qiu and Z. Huang, "Photodetectors of 2D materials from ultraviolet to terahertz waves," *Adv. Mater.*, vol. 33, no. 15, Apr. 2021, Art. no. 2008126, doi: 10.1002/adma.202008126.

[21] J. Tong, F. Suo, T. Zhang, Z. Huang, J. Chu, and D. H. Zhang, "Plasmonic semiconductor nanogroove array enhanced broad spectral band millimetre and terahertz wave detection," *Light, Sci. Appl.*, vol. 10, no. 1, Mar. 2021, Art. no. 58, doi: 10.1038/s41377-021-00505-w.

[22] J. Tong, W. Zhou, Y. Qu, Z. Xu, Z. Huang, and D. H. Zhang, "Surface plasmon induced direct detection of long wavelength photons," *Nature Commun.*, vol. 8, no. 1, Nov. 2017, Art. no. 1660, doi: 10.1038/s41467-017-01828-2.

[23] K. Yokota et al., "Surface metallic states in ultrathin Bi(001) films studied with terahertz time-domain spectroscopy," *Appl. Phys. Lett.*, vol. 100, no. 25, Jun. 2012, Art. no. 251605, doi: 10.1063/1.4729149.

[24] C. Clavero, "Plasmon-induced hot-electron generation at nanoparticle/metal-oxide interfaces for photovoltaic and photocatalytic devices," *Nature Photon.*, vol. 8, no. 2, pp. 95–103, Feb. 2014, doi: 10.1038/nphoton.2013.238.

[25] R. Sundararaman, P. Narang, A. S. Jermyn, W. A. Goddard III, and H. A. Atwater, "Theoretical predictions for hot-carrier generation from surface plasmon decay," *Nature Commun.*, vol. 5, no. 1, Dec. 2014, Art. no. 5788, doi: 10.1038/ncomms6788.

[26] J. Lloyd-Hughes et al., "Influence of surface passivation on ultrafast carrier dynamics and terahertz radiation generation in GaAs," *Appl. Phys. Lett.*, vol. 89, no. 23, Dec. 2006, Art. no. 232102, doi: 10.1063/1.2398915.

[27] Q. Song et al., "Optically tuned wide-band terahertz modulation, charge carrier dynamics and photoconductivity of femtosecond laser ablated titanium disulfide nanosheet devices," *IEEE J. Sel. Topics Quantum Electron.*, vol. 27, no. 3, pp. 1–6, May 2021, doi: 10.1109/JSTQE.2020.2996248.

[28] R. P. Prasankumar et al., "Carrier dynamics in self-assembled ErAs nanoislands embedded in GaAs measured by optical-pump terahertz-probe spectroscopy," *Appl. Phys. Lett.*, vol. 86, no. 20, May 2005, Art. no. 201107, doi: 10.1063/1.1923174.

[29] O. Ostroverkhova, D. G. Cooke, F. A. Hegmann, R. R. Tykwinski, S. R. Parkin, and J. E. Anthony, "Anisotropy of transient photoconductivity in functionalized pentacene single crystals," *Appl. Phys. Lett.*, vol. 89, no. 19, Nov. 2006, Art. no. 192113, doi: 10.1063/1.2387135.

[30] L. Viti, A. Politano, K. Zhang, and M. S. Vitiello, "Thermoelectric terahertz photodetectors based on selenium-doped black phosphorus flakes," *Nanoscale*, vol. 11, no. 4, pp. 1995–2002, Jan. 2019, doi: 10.1039/C8NR09060B.

[31] D. S. Ponomarev et al., "Sub-terahertz FET detector with self-assembled sn-nanothreads," *J. Phys. D, Appl. Phys.*, vol. 53, no. 7, Feb. 2020, Art. no. 075102, doi: 10.1088/1361-6463/ab588f.

[32] H. Xu et al., "$PtTe_2$-based type-II dirac semimetal and its van der Waals heterostructure for sensitive room temperature terahertz photodetection," *Small*, vol. 15, no. 52, Dec. 2019, Art. no. 1903362, doi: 10.1002/smll.201903362.

[33] (Jun. 14, 2019). *Product Description for Golay Cell*. Accessed: Jul. 25, 2023. [Online]. Available: http://www.eachwave.com/Product/054637111.html

[34] (Jun. 14, 2019). *Product Description for Bolometer*. Accessed: Jul. 25, 2023. [Online]. Available: http://www.eachwave.com/Product/456031513.html

[35] Q. Qiu and Z. Huang, "Photodetectors of 2D materials from ultraviolet to terahertz waves," *Adv. Mater.*, vol. 33, no. 15, Apr. 2021, Art. no. e2008126, doi: 10.1002/adma.202008126.

[36] W. Ma et al., "Ultrabroadband tellurium photoelectric detector from visible to millimeter wave," *Adv. Sci.*, vol. 9, no. 5, Feb. 2022, Art. no. e2103873, doi: 10.1002/advs.202103873.

[37] F. Teppe et al., "Room-temperature plasma waves resonant detection of sub-terahertz radiation by nanometer field-effect transistor," *Appl. Phys. Lett.*, vol. 87, no. 5, p. 52107, Aug. 2005, doi: 10.1063/1.2005394.

[38] Z. Huang et al., "Extreme sensitivity of room-temperature photoelectric effect for terahertz detection," *Adv. Mater.*, vol. 28, no. 1, pp. 112–117, Jan. 2016, doi: 10.1002/adma.201503350.

[39] Z. Lang, S. Qiao, and Y. Ma, "Fabry–Pérot-based phase demodulation of heterodyne light-induced thermoelastic spectroscopy," *Light, Adv. Manuf.*, vol. 4, no. 2, p. 23, 2023, doi: 10.37188/lam.2023.023.

[40] Y. Ma, T. Liang, S. Qiao, X. Liu, and Z. Lang, "Highly sensitive and fast hydrogen detection based on light-induced thermoelastic spectroscopy," *Ultrafast Sci.*, vol. 3, p. 24, Jan. 2023, doi: 10.34133/ultrafastscience.0024.

[41] Y. Zheng et al., "Numerical simulation of efficient solar absorbers and thermal emitters based on multilayer nanodisk arrays," *Appl. Thermal Eng.*, vol. 230, Jul. 2023, Art. no. 120841, doi: 10.1016/j.applthermaleng.2023.120841.

[42] S. Liang et al., "Tunable smart mid infrared thermal control emitter based on phase change material VO2 thin film," *Appl. Thermal Eng.*, vol. 232, Sep. 2023, Art. no. 121074, doi: 10.1016/j.applthermaleng.2023.121074.

[43] F. Qin et al., "Design of high efficiency perovskite solar cells based on inorganic and organic undoped double hole layer," *Sol. Energy*, vol. 262, Sep. 2023, Art. no. 111796, doi: 10.1016/j.solener.2023.111796.

[44] F. Wu, P. Shi, Z. Yi, H. Li, and Y. Yi, "Ultra-broadband solar absorber and high-efficiency thermal emitter from UV to mid-infrared spectrum," *Micromachines*, vol. 14, no. 5, p. 985, Apr. 2023, doi: 10.3390/mi14050985.

[45] R. Lai, P. Shi, Z. Yi, H. Li, and Y. Yi, "Triple-band surface plasmon resonance metamaterial absorber based on open-ended prohibited sign type monolayer graphene," *Micromachines*, vol. 14, no. 5, p. 953, Apr. 2023, doi: 10.3390/mi14050953.

[46] Z. Chen et al., "Graphene multi-frequency broadband and ultra-broadband terahertz absorber based on surface plasmon resonance," *Electronics*, vol. 12, no. 12, p. 2655, Jun. 2023, doi: 10.3390/electronics12122655.